Physics – Uspekhi **65** (6) 617 – 626 (2022)

INSTRUMENTS AND METHODS OF INVESTIGATION PACS numbers: **42.79. – e**, **78.55. – m**, 78.67.Hc

Three-dimensional fluorescence nanoscopy of single quantum emitters based on the optics of spiral light beams

I Yu Eremchev, D V Prokopova, N N Losevskii, I T Mynzhasarov, S P Kotova, A V Naumov

DOI: https://doi.org/10.3367/UFNe.2021.05.038982

Contents

Abstract. Far-field superresolution fluorescence microscopy (nanoscopy), awarded the Nobel Prize in Chemistry in 2014, has become one of the most powerful tools in multidisciplinary applications of photonics. In this paper, we discuss the technique of three-dimensional nanoscopy with the detection of transformed fluorescence images of single quantum emitters (using the example of semiconductor colloidal quantum dots, QDs). Nanoscale spatial resolution when reconstructing all three coordinates of single QDs is achieved by the instrumental modification of the point spread function using highly efficient light phase spatial modulators (diffractive optical elements, DOEs). DOE phase distributions, which ensure the formation of two-lobe light fields (with rotation of the intensity distribution during light propagation), were obtained on the basis of the optics of spiral light beams. The question of calculating DOEs that provide the best conversion efficiency of light beams is discussed. Theoretical and experimental analyses of the accuracy of the method were carried out depending on the experimental parameters: QD photoluminescence intensity, signal acquisition time, laser excitation power, and the instrumental function of the microscope objective. It is shown that, for the studied CdSeS/ZnS QDs, the accuracy of determining the coordinates can reach values of $\sim$ 10 nm at exposure times of $\sim$ 100 ms.

Keywords: luminescence, microscopy, nanoscopy, diffraction limit, spatial resolution, single molecule, quantum dot, point spread function, adaptive optics, diffractive optical element, Laguerre–Gauss modes, spiral beams, double-helix point spread function, DHPSF, quantum optics, nanodiagnostics, sensorics

I Yu Eremchev [1, 2, a], **D V Prokopova** [3], **N N Losevskii** [3], **I T Mynzhasarov** [2, 4], **S P Kotova** [3, b], **A V Naumov** [1, 2, 4, 5, c]

[1] Institute of Spectroscopy, Russian Academy of Sciences, ul. Fizicheskaya 5, 108840 Troitsk, Moscow, Russian Federation

[2] Lebedev Physical Institute, Russian Academy of Sciences, Troitsk Branch, ul. Fizicheskaya 11, 108840 Troitsk, Moscow, Russian Federation

[3] Lebedev Physical Institute, Russian Academy of Sciences, Samara Branch, ul. Novo-Sadovaya 221, 443011 Samara, Russian Federation

[4] Moscow Institute of Physics and Technology (National Research University), Institutskii per. 9, 141701 Dolgoprudny, Moscow region, Russian Federation

[5] Moscow State Pedagogical University, ul. Malaya Pirogovskaya 1, 119991 Moscow, Russian Federation

E-mail: [a] eremchev@isan.troitsk.ru, [b] kotova@fian.smr.ru, [c] a_v_naumov@mail.ru

Received 10 March 2021
Uspekhi Fizicheskikh Nauk **192** (6) 663 – 673 (2022)
Translated by V L Derbov

1. Introduction

Fluorescence nanoscopy (superhigh spatial resolution optical microscopy) with localization of single marker molecules (Single Molecule Localization Microscopy, SMLM) is a relatively new method for the characterization and diagnostics of condensed media and biological subjects. The high interdisciplinary and practical significance of this field has been confirmed by the awarding of the Nobel Prize in Chemistry in 2014 for these studies (together with another technique of far-field superresolution microscopy based on stimulated selective quenching of fluorescence) [1–3]. SMLM resolution is beyond the diffraction limit restricting classical optical microscopy and allows positioning individual point (quantum) emitters to a few nanometers. To date, the technique has been implemented at both room and cryogenic temperatures, which opened fundamentally new possibilities for biological studies [4], condensed state physics [5], and molecular spectroscopy [6].

One of the groundbreaking results in the SMLM development was methods of reconstructing all three coordinates

of a point light source. The most widespread idea in the development of 3D nanoscopy methods is to modify the point spread function (PSF) of the microscope optical system so that a change in the structure of the formed image can be unambiguously related to the longitudinal position of the source (i.e., with depth localization relative to the focal plane of the microscope objective lens). There are various approaches to modifying the microscope PSF. Thus, a simple (astigmatic) technique can be implemented by adding a cylindrical lens to the microscope optical system [7]. In recent years, with the development of adaptive optics, optical microscopy acquired great instrumental capabilities [8, 9]. Using phase-transforming spatial modulators of light fields, it is possible to transform the PSF in a specified way, for which numerical methods of calculation of the appropriate diffractive optical elements (DOEs) by seeking optimal superposition of Laguerre–Gauss modes are being intensely developed [10–15]. This approach is simple from the point of view of the analysis of the obtained images and possesses a relatively large depth of object localization preserving the accuracy of coordinate reconstruction.

In 2008, Pavani and Piestun [12] elaborated an original technique of PSF transformation into a two-lobe image, which rotates when changing the distance between a sample and an objective lens (i.e., when varying the source depth position relative to the microscope focal plane). The technique, called the double-helix point spread function (DHPSF), was based on the methods of analysis and synthesis of coherent light fields, successfully developed by Russian research schools at the Samara Branch of the Lebedev Physical Institute of the Russian Academy of Sciences (RAS) and the Image Processing Systems Institute of RAS (at present, Samara Branch of the Federal Scientific Research Center Crystallography and Photonics of RAS) [10, 11, 13, 15].

In 2009, the DHPSF technique was approved for the first time in an experiment on visualizing fluorescence images of single molecules [16], which initiated a line of research on three-dimensional fluorescence DHPSF nanoscopy. To date, the technique has demonstrated a high potentiality for reconstructing the three-dimensional structure of objects with nanoscale spatial resolution both at room temperature for biophysical applications [17] and at cryogenic temperatures when detecting single molecules in solid matrices [5].

Now, DHPSF nanoscopy is actively developing in several directions. First, it is necessary to develop methods for calculating DOEs with optimal parameters, such as the efficiency of light field conversion and the DOE operating range, as well as taking into account the characteristics of microscope optical elements [15]. Second, the problem of image recognition requires the development of special algorithms and software to process large arrays of information [18, 19], including the use of machine learning algorithms [20]. Finally, there is an expanding range of emitting nanoobjects, the study of which requires involving the instrumental capabilities of 3D nanoscopy. So, among various nanoemitters, which at present are of great interest for science and technology, a special place is occupied by low-dimensional semiconductor structures — quantum wells, wires, and dots [21–23]. The spectroscopy and microscopy of single quantum dots (QDs) in various media often require high-precision spatial localization [24], due to which careful experimental testing is necessary for applying the DHPSF technique to such objects.

The present paper considers theoretical and experimental grounds of the DHPSF nanoscopic technique. The results of computer calculations of original phase diffractive optical elements based on two-lobe spiral beams are presented, including those obtained with the instrumental function of the microscope objective lens taken into account. Experiments on the 3D nanoscopy of single colloidal CdSeS/ZnS QDs are carried out and the issues of accuracy of three-dimensional localization of such quantum emitters are discussed in detail.

2. Modifying the point spread function using the double-helix scheme: experimental technique using adaptive optics

2.1 Description of the experimental setup

The setup is a self-made luminescence microscope optimized for experiments on three-dimensional localization microscopy with single emitting objects: single molecules, quantum dots, and color centers in diamonds [25]. The main difference between the experimental setup used and a conventional luminescence microscope is the presence of an additional DOE in the optical registration scheme of the microscope (Fig. 1). In this experiment, the light beams formed by the microscope objective for each of the 'point' sources are transformed into light fields with two expressed intensity maxima (so-called two-lobe fields) that rotate in the transverse plane in the course of propagation (see inset in Fig. 1; see also Fig. 3 below). Full rotation of the light field occurs at an angle determined by the rotation parameter θ_0 of the spiral light beam used as an initial approximation when calculating the DOE. In the present paper, we studied DOEs based on a spiral beam with the rotation parameter $\theta_0 = -2$ (full rotation at 180°) [11]. Rotation of the two-lobe field ($\Delta\alpha$) occurs mainly near the focal planes of the image at a characteristic distance of the order of the Rayleigh length (Z_R). At a fixed position of the plane of registration, the two-lobe image has a definite angle of rotation (as shown in Fig. 1). When moving the point object near the focal plane of the microscope objective, the angle changes, since the image plane is displaced relative to the plane of registration. This is exactly what makes it possible to determine the longitudinal coordinate of a point object in three-dimensional nanoscopy. The rate of light field rotation, $1/k' = \mathrm{d}\alpha/\mathrm{d}z$, defined as the ratio of the increment of the angle ($\mathrm{d}\alpha$) to the increment of the distance ($\mathrm{d}z$) along the optical axis near the image plane, depends on the Rayleigh length Z_R and the rotation parameter θ_0. Then, in the linear region, the rotation rate can be expressed as follows: $1/k' = \Delta\alpha/Z_R = 4(\mathrm{NA})^2\Delta\alpha/\pi\lambda M^2$, where λ is the wavelength, NA is the numerical aperture of the optical system (microscope objective), M is the transverse magnification of the microscope, and $\Delta\alpha$ is the total angle of rotation at the Rayleigh length. The longitudinal displacement of a point object near focal plane Z is related to the longitudinal displacement of the image z via the longitudinal magnification of the microscope, $z = ZM^2$; therefore, the rate of image rotation is $1/k = \mathrm{d}\alpha/\mathrm{d}Z = (\mathrm{d}\alpha/\mathrm{d}z)M^2 = 4(\mathrm{NA})^2\Delta\alpha/\pi\lambda$. Below, we will use exactly this rate and its reciprocal k, since it relates the image rotation angle to the distance between the objective focal plane and the point object and is directly measured in the experiment. It is seen that this rate depends on the numerical aperture of the microscope objective, the wavelength, and the full rotation

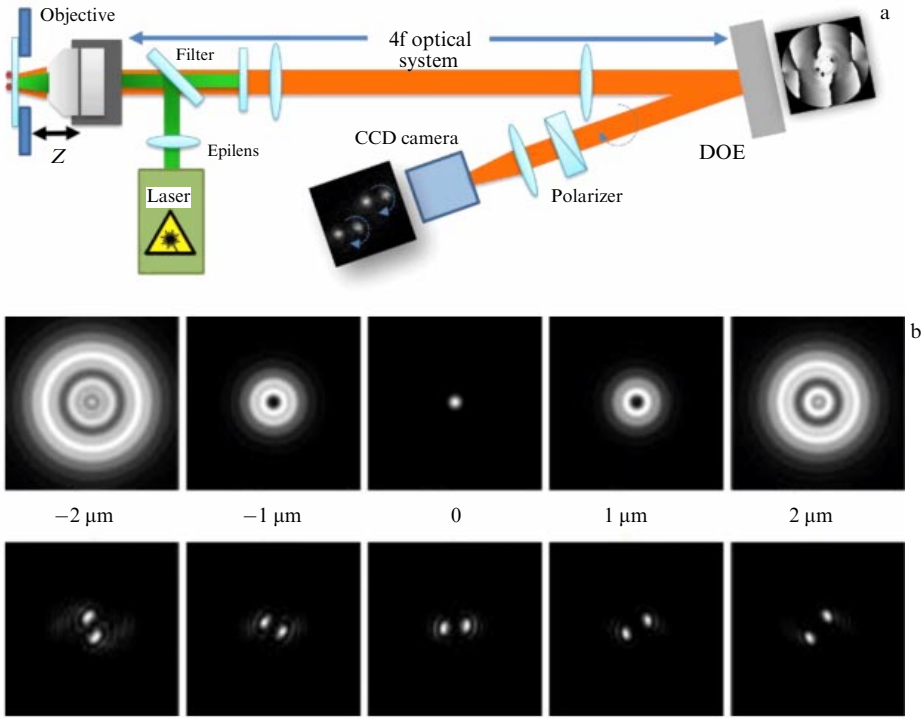

Figure 1. (a) Schematic diagram of the setup, a luminescence 3D nanoscope with instrumental modification of the point spread function using the double-helix scheme. (b) Calculated images of an ideal point source of radiation at five different distances from the focal plane of the microscope objective (from −2 to 2 μm) recorded by a conventional microscope (upper row of images) and the corresponding two-lobe images obtained by modification of the point spread function using the double-helix scheme (lower row of images).

angle at the Rayleigh length, but is independent of the microscope magnification.

To transform light beams, we used a spatial liquid crystal phase modulator, Holoeye Pluto BB, allowing us to vary the phase incursion of linearly polarized light independently for each of 1920 × 1080 pixels (8 μm in size) of a liquid crystal matrix. The polarization state required to illuminate the modulator was prepared using a linear polarizer (Thorlabs, USA).

The image in the microscope was formed by a Carl Zeiss immersion objective (100×, 1.3NA) and a system of lenses consisting of a 4f scheme and the objective of a CCD camera, which overall yielded a 93-fold optical magnification. The transverse resolution of the microscope was about 240 nm at the wavelength of QD luminescence (630 nm). The phase modulator was located in the focal plane of the 4f scheme of the microscope, conjugated with the exit pupil of the microscope objective. The microscope optical scheme geometry was optimized to minimize the angle of beam incidence on the phase modulator in order to reduce errors related to the spatial phase transformation of the incident beams. A piezoelectric scanner (NanoScanTech, Russia) that allowed displacing the microscope objective with nanoscale precision in the optical axis direction was used for high-accuracy measurement of the distance between the focal plane of the objective and the sample. The calibration of capacitive sensors of piezoelectric scanner displacement was implemented using a high-precision electronic micrometer, the Mahr Extramess 2000 (division value 0.2 μm, margin of error 0.3 μm).

A Coherent CR 599 wavelength-tunable dye laser at a wavelength of 580 nm excited the QD. The power density of the exciting radiation in the sample plane varied within the range from 50 to 200 W cm^{-2}. In addition, in a number of experiments, a TOPOL femtosecond optical parametric oscillator (Avesta) was used with the following parameters: second harmonic of the idle signal of the parametric oscillator at a wavelength of 580 nm, repetition rate of 1 MHz (rarefied by means of an electrooptic light modulator), laser pulse duration of $\sim$ 1 ps, energy density in the pulse from 10 to 280 μW cm^{-2}.

Luminescence images of quantum dots were recorded using a high-sensitivity cooled Andor Luca CCD camera. The measurement of luminescent trajectories was carried out by means of an avalanche photodiode EG&G SPCM 200 PQ, operating in the photon counting mode. The exposure time of one frame of the camera for recording two-lobe images varied from 100 to 500 ms for single QDs and from 10 to 400 ms for 'point' QD agglomerations. Band-pass interference filters (Semrock) were used to eliminate scattered laser radiation.

2.2 Subjects of study and sample preparation

To demonstrate the capabilities of the 3D DHPSF nanoscopy technique, semiconductor luminescent nanocrystals were used — colloidal core/shell CdSeS/ZnS QDs (Sigma Aldrich) with the maximum of luminescence at a wavelength of 630 nm. Individual QDs were deposited on a weakly luminescent thin glass substrate. The surface concentration was chosen such that the images of single QDs would not overlap in the microscope (less than 1 QD per μm^2). At the same time, on the sample it is possible to find fragments containing 'point' agglomerations (with a size smaller than the diffraction limit), consisting of a large number of QDs. Such objects were also interesting for the present study, since they played the role of a model of a photostable 'point' emitting object with an intensity several times higher than that of single QD

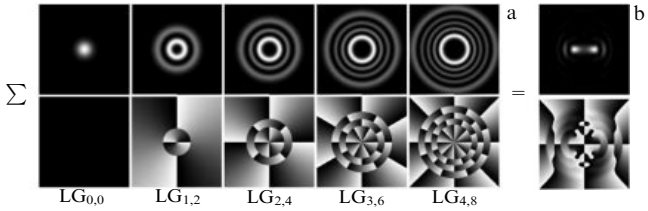

Figure 2. (a) Five Laguerre–Gauss modes ($LG_{0,0}$, $LG_{1,2}$, $LG_{2,4}$, $LG_{3,6}$, $LG_{4,8}$) used as an initial approximation in the DOE calculation for transforming the point spread function according to the double-helix scheme. (b) Superposition of the above five Laguerre–Gauss modes composing a double-helix beam (upper row — intensity distributions in grades of grey color, lower row — corresponding phase spatial distributions for the converting DOE).

luminescence in the bright state. To prepare the samples, we used a self-made spin coater (horizontal centrifuge): a drop of colloid solution of QDs in toluene was placed on a spinning glass substrate to distribute the QDs over the plate. The surface concentration was varied by changing the concentration of QDs in the solution.

2.3 Calculation of a diffractive optical element

To create a DOE that forms a rotating image, it is convenient to address the light fields that possess such a property. A distinctive feature of spiral beams is the rotation of intensity distribution in the course of propagation. Among the entire variety of spiral beams, those with an intensity distribution having two principal maxima — two-lobe spiral beams — are in demand [11, 13, 26]. Since the methods of spiral beam formation have a low energy efficiency, to modernize the PSF of the microscope system, a DOE based on a two-lobe spiral beam was used, which efficiently converted the incident light beam into a two-lobe light field (Fig. 2).

The procedure of the element calculation is a modified Gerchberg–Saxton algorithm, in which the field correction occurs not only in single Fourier plane but also in a few planes equispaced from it. This feature ensures the calculation of the phase of the element forming a specified spatial structure of the field. The proposed algorithm is described in detail in Ref. [27]. One iteration of the algorithm consists of performing direct and inverse Fresnel transformations among N reference planes, in which the correction of the field intensity distribution occurs. As an initial approximation, used were the phase distribution of a two-lobe spiral beam of light, which is a superposition of five Laguerre–Gauss modes,

$$F = \mathrm{LG}_{0,0} + \mathrm{LG}_{1,2} + \mathrm{LG}_{2,4} + \mathrm{LG}_{3,6} + \mathrm{LG}_{4,8}\,,$$

and an intensity distribution uniform over the element aperture (see Fig. 2).

Earlier in the course of studies it was found that amplitude and phase distortions substantially affect the field formed by the obtained element and introduce noises into the recorded two-lobe image [28, 29]. In turn, this may cause an error in the localization of the emitting object. Therefore, to optimize the calculated DOE for operating with a certain microscope objective lens, the pattern formed by the objective in the Fourier plane where the element will be placed (Fig. 3) is used as the initial approximation. In the process of such optimization, the DOE for operating with the Carl Zeiss (100×, 1.3NA) immersion objective was calculated. In this element, the efficiency of conversion of the incident radiation into the two-lobe field amounts to 86% and exceeds analogous values for DOEs obtained earlier [15]. The phase distributions of the elements are presented in Fig. 3d, e.

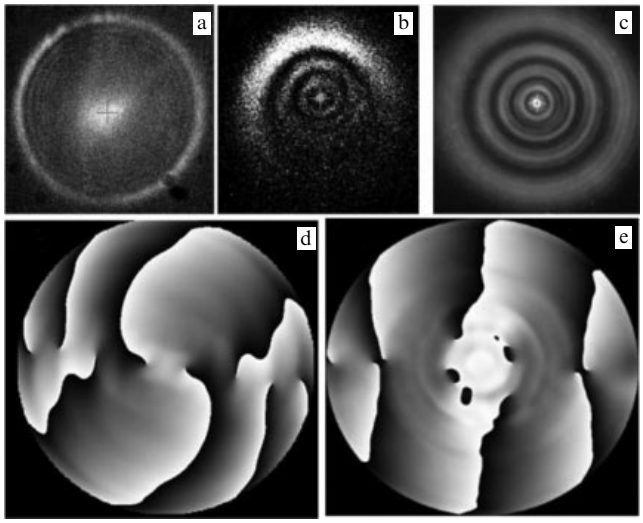

Figure 3. Examples of luminescence intensity spatial distributions from single point objects in parallel beams produced by high-aperture microscope objectives: (a) immersion CFI Nikon 60×, 1.2NA, (b) CF Nikon 100×, 0.95NA, (c) Carl Zeiss 100×, 1.3NA. Phase spatial distributions are encoded in grades of grey (black — 0, white — 2π) (so-called phase masks): (d) non-optimized, (e) optimized for the intensity distribution shown in Fig. 3c.

3. Experimental results and discussion

3.1 Instrumental function of the objective

In the present paper, the precision of longitudinal coordinate measurements using two different DOEs was compared. The first DOE was calculated for a uniform distribution of the incident beam intensity. The second was calculated for a nonuniform intensity distribution close to that (Fig. 3c) produced by the microscope objective lens (Carl Zeiss 100×, 1.3NA) used. It should be noted that we tested several microscope objective lenses with a high numerical aperture for use in three-dimensional localization high-resolution microscopy. For each of them, we determined experimentally the luminescence intensity distribution in the phase modulator plane, which was produced by the beam from a single point object (QD) placed in the focal plane of the microscope objective lens. Figures 3a–c show examples of intensity distributions for the chosen objective (Fig. 3c) and two other objectives (Fig. 3a, b).

It was found that, when using different objectives, the intensity distribution produced is not suited to the considered technology because of inefficient DOE filling. According to the algorithm described in Section 2.3, the calculations of DOEs were carried out for two cases: the non-optimized case of ideally uniform illumination (Fig. 3d) and the optimized version (Fig. 3e) taking into account the intensity distribution produced by the particular microscope objective (Fig. 3c).

3.2 Calibration of the double-helix scheme with various diffractive optical elements

Using the calculated DOEs, the two-lode images of single QDs were recorded at various (controlled with nanoscale precision) depth positions with respect to the focal plane of

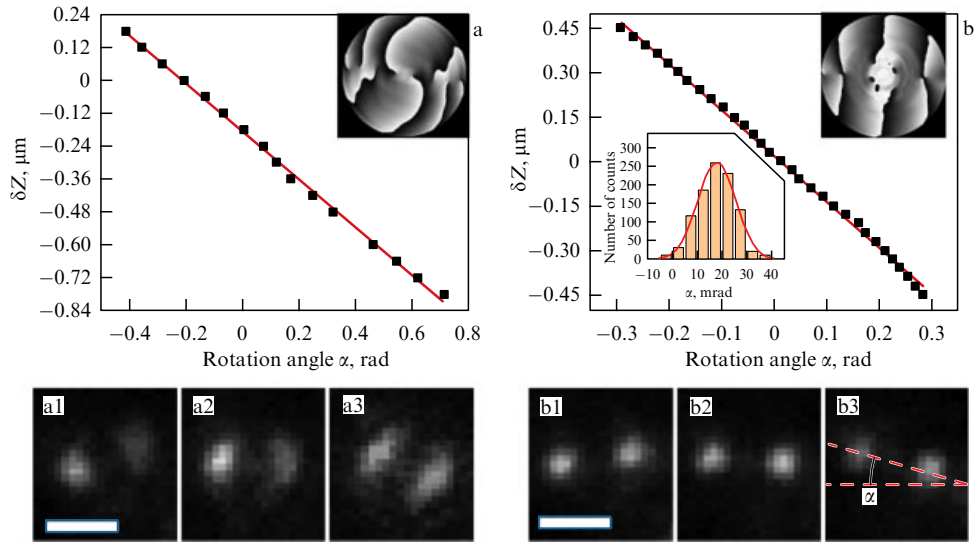

Figure 4. Calibration curves for non-optimized (a) and optimized (b) DOEs. Examples of modified images of point sources (two-lobe images) at various distances between the point source and the microscope objective focal plane for non-optimized (a1–a3) and optimized (b1–b3) DOEs. Scale is similar in all figures; length of white rectangles corresponds to 1 μm.

the microscope objective. Figure 4 shows examples of modified images of point sources (two-lobe images) at various distances between the point source and the focal plane of the microscope objective. In both cases, the change in the distance is seen to cause a rotation of the two-lobe image.

In the optimized DOE case (Fig. 4b1–b3), the two-lobe image consists of two symmetric spots, close in shape to the two-dimensional Gaussian function. The characteristic dimensions of the lobes, $\sigma_{PSF} = 259$ nm (a root-mean-square deviation, RMSD, derived from approximation by the two-dimensional Gaussian function), are close to the image size of a point object without using a DOE, $\sigma_{PSF} = 234$ nm.

In the case of a non-optimized phase mask (Fig. 4a1–a3), the lobes have an asymmetric shape that changes when the image is rotated. In this case, the average characteristic width of the lobes is 1.3 times greater than in the case of the optimized mask.

To relate the two-lobe image rotation angle α (shown in Fig. 4b3) and the distance from the point object to the objective focal plane Z, the DOE calibration procedure was carried out. For this purpose, the microscope objective was sequentially shifted (near the focus) along the optical axis with a step of 30 and 60 nm (for the optimized and non-optimized DOE, respectively), and the two-lobe images were recorded. An electromechanical piezo manipulator provided movement control with an absolute accuracy of no worse than 1 nm. At each movement step a series of 100 sequential measurements of two-lobe images was performed with a frame exposure of 200 ms to improve the accuracy of the rotation angle determination. To process the images, a program was used based on algorithms of approximation of individual image lobes with two-dimensional Gaussian functions [5, 6]. As a result of the approximation, a set of parameters is obtained for each of the lobes: the root-mean-square deviations, σ_{PSF} (lobe width), and the transverse lobe coordinates (x, y) reconstructed to a sub-diffraction accuracy. The reconstructed coordinates were used to determine the tangent of the image rotation angle, $\tan\alpha = (y_2 - y_1)/(x_2 - x_1)$, and the center of gravity of the two-lobe image, $X = (x_1 + x_2)/2$, $Y = (y_1 + y_2)/2$. For each depth of the point source location with respect to the focal plane of the microscope objective (the position of the piezo scanner being fixed), a distribution of angle α values was constructed and approximated with a Gaussian function (see the example in the inset in Fig. 4b). The center of each of these distributions was used as the found value of angle α at the given value of Z to draw the calibration curve $Z(\alpha)$. Figure 4a, b shows the calibration dependences obtained for the non-optimized and optimized masks, respectively. The rotation rate of the two-lobe image amounted to $k = 1.5$ μm rad^{-1} (optimized) and $k = 0.9$ μm rad^{-1} (non-optimized).

Having obtained the calibration curves, we carried out a series of experiments to estimate the accuracy of the longitudinal coordinate reconstruction. As a parameter of accuracy, we used the root-mean-square deviation σ_z for the values of the reconstructed coordinates obtained in a series of experiments with fixed parameters. Two type of experiments were performed. In the first, the accuracy $\sigma_z(N)$ was studied depending on the variation in the number of photons N that produce the two-lobe image at fixed position Z of the piezo scanner (fixed rotation angle α of the two-lobe image). In the second case, the accuracy $\sigma_z(\alpha)$ was studied depending on the scanner position Z (image rotation angle α) at a fixed number of photons.

3.3 Accuracy of reconstructing the spatial coordinates of point emitters depending on various factors

In Fig. 5d–f, examples of distributions for the reconstructed coordinates X, Y, Z, obtained in a series of 100 sequential measurements at fixed values of α and N, are shown, and the corresponding values of RMSs $(\sigma_x, \sigma_y, \sigma_z)$ are indicated. The spread in each coordinate is determined by three contributions. The first one is related to the shot noise in the number of photons hitting individual pixels of the camera, corresponding to the two-lobe image. This leads to shape variations in the two-lobe images and, as a consequence, to variations in the reconstructed coordinates.

For symmetric lobes with a Gaussian shape, this contribution to the reconstruction accuracy of the two-lobe image center-of-gravity transverse coordinates can be

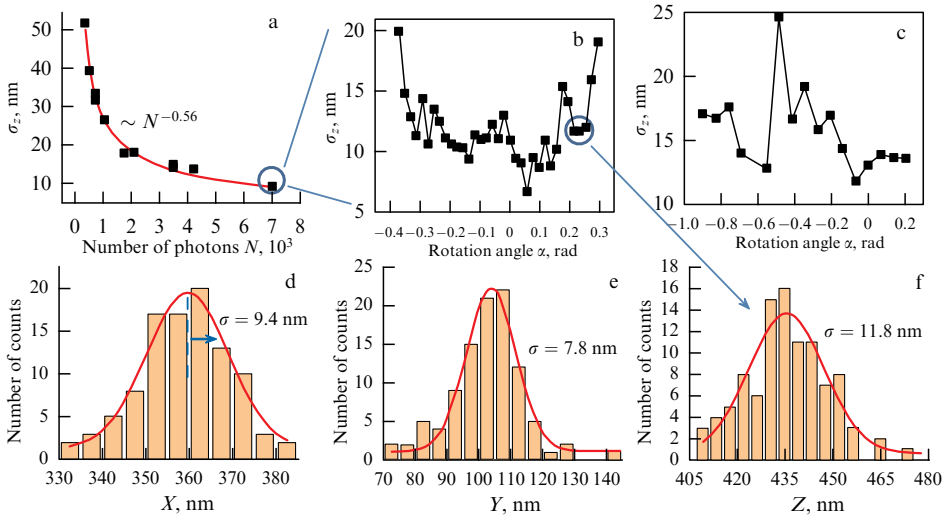

Figure 5. Reconstruction accuracy for the longitudinal coordinate of a single point object. (a) Dependence of longitudinal coordinate reconstruction accuracy σ_z on the number of photons forming the two-lobe image for rotation angle $\alpha \sim 0$ (the point object is at the focus) using the optimized DOE. Dependence has the form of a reciprocal root function. (b) Dependence of the longitudinal coordinate reconstruction accuracy σ_z on the rotation angle α in the case of an optimized DOE for the region marked in Fig. 5a (7000 photons). (c) Similar dependence for the non-optimized DOE (7000 photons). (d–f) Example of distribution of the values of reconstructed (d, e) transverse and (f) longitudinal coordinates of a quantum dot, whose fluorescence image has been measured repeatedly.

described by the expression (not taking into account the possible noise pedestal)

$$\sigma_{x,y} = \frac{\sigma_{\mathrm{PSF}}}{\sqrt{N}}\,, \tag{1}$$

where σ_{PSF} is the characteristic lobe width, and N is the number of photocounts forming the two-lobe image. A more precise expression takes into account the signal-to-noise ratio and the parameter characterizing the spatial discreteness of the image [30]. For the case shown in Fig. 5d, e ($N = 7000$, $\alpha \sim 0.2$ rad), an estimate using the above expression is $\sigma_{x,y} \sim 3$ nm, which is several times smaller than the RMS obtained experimentally.

In the case of small rotation angles, the random error for an arbitrary coordinate is simply related to the errors in the transverse coordinates:

$$\sigma_z = \frac{2k\sigma_{x,y}}{d} = \frac{2k\sigma_{\mathrm{PSF}}}{d\sqrt{N}}\,, \tag{2}$$

where k is the two-lobe image rotation rate, and d is the distance between the lobe centers. An estimate for the optimized DOE at $N = 7000$ is $\sigma_z = 10.4$ nm, which is close to the values obtained experimentally (Fig. 5b, f).

The second contribution is due to the drift of the point emitter image, e.g., because of the Brownian motion of the emitter in a viscous medium or mechanical instability of the microscope optical elements. In the experiments carried out, the drift was due to the mechanical instability of the microscope focusing system, giving rise to a similar drift of all point emitters in the microscope field of view. Figure 6b shows an example of time evolution of the reconstructed coordinate Z of a point emitter drifting quasilinearly along the z-axis with a velocity of 0.3 nm s^{-1}. This effect broadens the distribution of coordinates and, accordingly, increases the measured error. To allow for this parasitic effect, a procedure of drift velocity estimation and coordinate shift compensation was performed.

The third contribution to the error is caused by the fact that the emitters used in the experiment are point agglomerations consisting of a small number of QDs. Independent blinking of QDs causes a spatial redistribution of the luminescence pattern at a subdiffraction level, which gives rise to a shift of the agglomeration emission center. Figure 6d shows examples of time evolutions of the reconstructed transverse coordinates (X, Y) of the two-lobe image center of gravity. We see that the reconstructed coordinates experience both smooth and jump-like changes within the spatial range of a few tens of nanometers. No such effect is observed in the case of single QDs, and the behavior is unique for each of the simultaneously measured agglomerations. This testifies to the fact that the described effect is not due to mechanical instability of the microscope or hypothetic drift of individual agglomerations over the glass substrate.

It should be noted that it is exactly this contribution that gives rise to the substantial difference with the error estimate obtained for transverse coordinates (X, Y) using Eqn (1) from the experimental values (by 2–3 times for $N = 7000$). For the longitudinal coordinate, the difference turned out to be small, which, on the one hand, is due to a substantially greater value of the 'minimum' σ_z (from Eqn (2)) and, on the other hand, is because of the agglomeration planar geometry (extended in the x, y plane), both resulting in the absence of recorded displacement of the emission center along the Z-axis. Thus, the obtained results show that from the point of view of studying the properties of the longitudinal coordinate conversion into the image rotation, the used point agglomerations of QDs can serve as a good model of a point object.

Figure 5b shows examples of the dependence of σ_z on the image rotation angle α for the optimized and non-optimized DOE, respectively, at a fixed number of photons $N = 7000$. It is seen that, in the case of optimized DOE, the accuracy of coordinate reconstruction is on average 1.5 times higher. At the edges of the dependence $\sigma_z(\alpha)$ for the optimized DOE, the error σ_z grows. This is because, at large absolute values of the angle, the efficiency of the beam conversion into a rotating two-lobe image decreases [15]; in these cases, a substantially greater proportion of light is redistributed into additional diffraction maxima, effectively increasing the noise pedestal

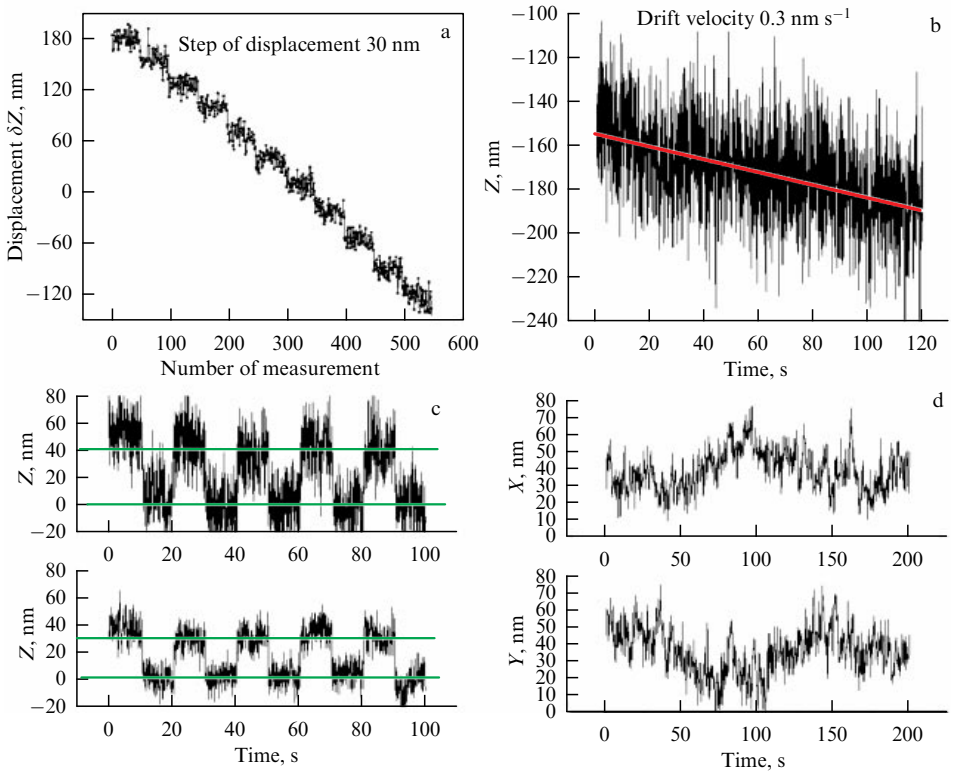

Figure 6. Examples of recording the movement of a single point emitter along the z-axis using the optimized DOE. (a) Experiment with controlled displacement of the sample (with a step of 30 nm) along the z-axis by means of a piezo scanner. At each step of the piezo scanner, 100 measurements were carried out with the acquisition time of 200 ms. Z-coordinate reconstruction accuracy corresponds to $\sim$ 11 nm (Fig. 5b). (b) Observation of quasilinear drift of the point emitter (together with the glass substrate) along the z-axis related to the mechanical instability of the microscope focusing system. Drift velocity is ~ 0.3 nm s^{-1}. (c) Examples of recording cyclic movement of the point emitter by means of a piezo scanner by 30 nm for the optimized phase mask (bottom) and by 40 nm for the non-optimized mask (top). (d) Examples of time evolution of the reconstructed transverse coordinates of the two-lobe image center-of-gravity with the observed displacement of the emission center in the blinking agglomeration of dots: X (top), Y (bottom). Exposure time in both examples is 200 ms; mean number of photocounts in the two-lobe image $N = 7000$.

(reducing the signal-to-noise ratio). Moreover, in this case, a deformation of the two-lobe image occurs. It should also be noted that a direct comparison of the Z coordinate reconstruction accuracy for the two considered DOEs using Eqn (2) is impossible. Indeed, in the case of the non-optimized DOE (as well as the optimized DOE for large angles), the lobe images are asymmetric and are on a higher noise pedestal. In this case, Eqn (2) is not applicable to describe the error.

Figure 5a shows the dependence of the reconstruction accuracy of the single point object longitudinal coordinate on the number of photocounts N for the angle $\alpha \sim 0$ (the point object is near the microscope focal plane) when using the optimized DOE. The obtained curve corresponds to a reciprocal root dependence on the number of photocounts N, which agrees well with expression (2). We did not plot such dependences for the image center-of-gravity coordinates X, Y since they include an additional contribution to the error discussed above. In the case of a single quantum dot, the dependence of the reconstruction accuracy for the transverse coordinates X, Y has a similar form [25].

To demonstrate the possibility of reconstructing longitudinal coordinates with an accuracy of $\sim$ 11 nm in a single measurement (with $N = 7000$), Fig. 6 shows the time evolution of the reconstructed longitudinal coordinate Z in the experiment, in which the sample was sequentially moved by the piezo drive with a step of 30 nm, and 100 images were measured at each step. The mean number of photocounts in each image was close to 7000. We see that the time evolution is presented by a stepped plot with distinctly seen steps. The width of each 'shelf' is determined by the accuracy of coordinate reconstruction in a single measurement. Figure 6c also shows examples of recording the cyclic movement of a point emitter along Z by a distance of 30 nm for the optimized phase mask (bottom) and by 40 nm for the non-optimized mask (top). The presented example demonstrates the difference in the coordinate reconstruction accuracy using the studied DOEs.

3.4 3D nanoscopy of single colloid semiconductor quantum dots exhibiting the effect of luminescence blinking

To demonstrate the possibility of using optimized DOEs with single colloidal CdSeS/ZnS quantum dots, a number of experiments have been carried out. Figure 7c shows two-lobe luminescence images of single colloidal CdSeS/ZnS QDs in a microscope field of view. The power density of the exciting radiation was ~ 100 W cm^{-2}, and the acquisition time was 500 ms. Figure 7a shows an example of a blinking luminescence trajectory of a single QD, marked in Fig. 7c. The QD luminescence intensity changes (blinks) because of the variation in the proportion between the rates of radiative and non-radiative relaxation of an electron-hole pair [31–33]. From the point of view of superresolving localization microscopy, the QD blinking leads to a change in the number of photocounts forming the two-lobe image and, therefore, to

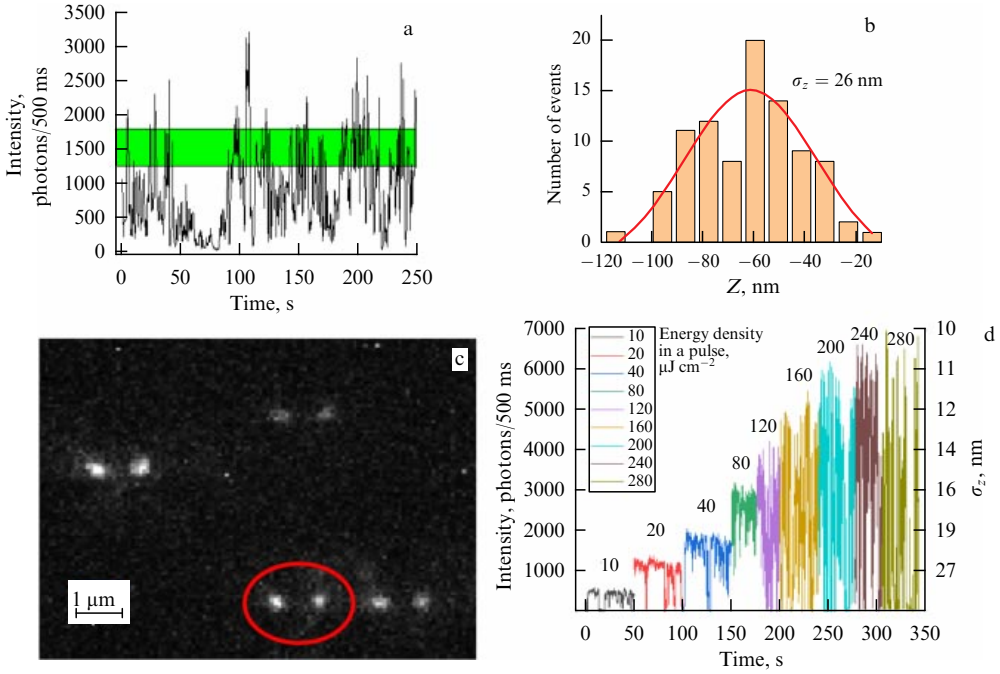

Figure 7. (Color online.) Reconstruction of the longitudinal coordinate of single CdSeS/ZnS quantum dots using an optimized DOE and evolution of the luminescence trajectory with an increase in the intensity of the pulsed laser excitation. (a) Example of blinking luminescence trajectory for a single QD, the two-lobe image of which is marked with an oval in Fig. 7c. Power density of the exciting radiation is ~ 100 W cm^{-2}, acquisition time is 500 ms. (b) Distribution of the longitudinal coordinate z corresponding to the luminescence intensity range with the mean number of photocounts $N = 1500$. (c) Luminescence image of the microscope field of view containing two-lobe images of single colloid CdSeS/ZnS QDs. (d) Evolution of a blinking trajectory measured without a spatial phase modulator as the energy density in a laser excitation pulse increases from 10 to 280 μJ cm^{-2}. Wavelength is 500 nm, repetition rate is 1 MHz, pulse duration is 1 ps. Right-hand scale of the plot demonstrates the calculated accuracy of the reconstructed coordinates in an ideal case (for 100% DOE conversion efficiency) corresponding to different intensities of laser excitation of a single QD.

a variation in the coordinate reconstruction error σ_z in sequential measurements at unchanged power density of the exciting laser radiation. Figure 7b presents the distribution of the longitudinal coordinate values corresponding to a range of luminescence intensities with the mean number of photocounts $N = 1500$ (Fig. 7a). The longitudinal coordinate reconstruction accuracy for this range amounted to $\sigma_z = 26$ nm, which is close to the estimate obtained from expression (2), ~ 23 nm for $N = 1500$. For the moments of time on the fluorescent trajectory corresponding to the maximum luminescence values of $N \sim 3000$ photocounts/500 ms (Fig. 7a), the accuracy must correspond to the value of $\sigma_z \sim 18$ nm, which is an order of magnitude higher than the values determined by the diffraction limit.

We now proceed to the issue of how to increase the accuracy of measuring coordinates using single QDs. Naturally, when we increase the acquisition time, we increase the number of photocounts N; however, in this case, the time resolution, which is important for tracking the particles, also decreases. Moreover, the error of coordinate determination due to drift (studied or parasitic) also decreases. Therefore, this parameter cannot be varied within broad limits and in each particular case should be chosen based on the task requirements. In addition to the exposure time, the number of luminescence photons can be increased at the expense of increasing the power density of the exciting radiation. In this case, the restrictions from above also apply. They are associated with the quantum dot saturation and blinking processes. The saturation is related to the domination of radiationless Auger recombination under an increase in the probability of QD excitation to states with more than one electron-hole pair. This leads to a decrease in the quantum yield of the luminescence with the growth of excitation intensity. The maximum intensity will depend on the luminescence lifetime (~ 25 ns in the bright state for a QD) as well as on the type of laser excitation of a QD (pulsed or cw).

In addition to the saturation effect, with an increase in the power density of the exciting radiation, photoactivation of QD blinking occurs (including due to an increase in the probability of Auger transitions): the probability of transitions from bright to dark state increases. Figure 7d shows the evolution of blinking of a single QD upon increasing the intensity of the pulsed lased excitation (wavelength 580 nm, repetition rate 1 MHz, pulse duration 1 ps). We see that, with increasing pumping, a passage occurs from luminescent trajectories with rare transitions to the dark state to jagged trajectories with multiple intermediate levels of luminescence intensity. In addition, the maximum luminescence intensity in the trajectory gradually goes to a plateau (saturation). Note that the effect of QD blinking causes certain difficulties in using single QDs in experiments where a prescribed accuracy of coordinate reconstruction is required. On the other hand, this effect allows resolution of more than one point emitter within a diffraction-limited region (to determine coordinates with subdiffraction accuracy) at the expense of separate recording of the centers of single QDs [19].

Finally, an important parameter that affect the number of photocounts in the two-lobe image is the total efficiency of the beam conversion into the two-lobe image, $\eta = k_{\text{pol}}\, k_{\text{dif}}\, k_{\text{conv}}$. In this formula, k_{pol} is the coefficient allowing for the loss at the linear polarizer, which in the case of single QDs (emission of light with natural polarization) amounts to $k_{\text{pol}} = 0.5$;

$k_{dif} = 0.6$ is the coefficient of reflection into the zeroth order related to the diffraction on the internal pixel structure of the spatial phase modulator; k_{conv} is the efficiency of beam conversion by a phase mask (80% for the optimized DOE and 65% for the non-optimized one). The coefficient k_{conv} [15] is a ratio of the number of photocounts in the two-lobe image formed by the phase mask to the number of photocounts in the 'classical' diffraction image of the same source. Therefore, the total efficiency of the optimized DOE is $\eta = 0.2$, i.e., $\sim 20\%$ of photons recorded in an experiment without using a phase modulator hit the two-lobe image. Figure 7d (right scale of the plot) presents the calculated values of the coordinate reconstruction accuracy for a single QD at an acquisition time of 100 ms and DOE efficiency of 100% corresponding to various intensities of laser excitation of a single QD (including the saturation mode). An increase in the total efficiency (approaching 100%) is possible by replacing the liquid crystal spatial phase modulators with steady state lithographed DOEs, allowing the conversion of both orthogonal polarizations of light at once.

4. Conclusion

The present paper considers the technique of three-dimensional localization microscopy with superhigh spatial resolution based on detecting transformed fluorescence images of single quantum emitters (semiconductor quantum dots). The nanoscale spatial resolution in the reconstruction of all three coordinates of single QDs is achieved by modifying the point spread function of the system using spatial phase convertors of the optical field (diffractive optical elements). These elements are based on the optics of spiral light beams and produce two-lobe optical fields with the intensity distribution rotating in the course of propagation [12, 16]. We have calculated new DOEs that provide high efficiency of light beam conversion within the ~ 500-nm range of the point object longitudinal displacements, which corresponds to the tasks of far-field nanoscopy using a high-aperture microscope objective.

Theoretical and experimental analyses of the coordinate reconstruction accuracy for single point emitters are being carried out. The nature of noises making the main contribution to the error of coordinate determination is considered, as are the influence of the two-lobe image shape, the rotation parameter, the number of image-forming photocounts, and the distance between the point object and the microscope focal plane on the accuracy of determining point emitter coordinates. The accuracy of reconstructing the longitudinal coordinate is shown to decrease at the edges of the range of the two-lobe image rotation angles and to have a reciprocal root dependence on the number of photocounts. Two DOEs are compared experimentally, the first one optimized for operating within a narrow range of longitudinal coordinate variation (~ 600 nm) allowing for the field distribution in the beam generated by a wide-aperture microscope objective from a point source of radiation. The second DOE was aimed to operate within a wider range of longitudinal coordinate variation (~ 1 μm) with a beam having a uniform field distribution. It is shown that the accuracy of determining the longitudinal coordinate is on average 1.5 times higher in the case of optimized DOEs, in spite of the fact that the two-lobe image rotation rate parameter turned out to be higher in the case of non-optimized DOEs. This result is associated with the two-lobe image asymmetry affecting the coordinate reconstruction accuracy in the case of non-optimized DOEs, larger characteristic widths of the lobes, as well as lower conversion efficiency. The possibility of nanoscale tracking of a point emitter in the longitudinal direction with an accuracy in the range up to 500 nm is experimentally demonstrated.

Experiments with singular CdSeS/ZnS quantum dots were carried out. The possibility of using an optimized DOE for the three-dimensional determination of the spatial position of single QDs with nanometer accuracy in all three coordinates was demonstrated. Estimates of the longitudinal coordinate reconstruction accuracy for a single CdSeS/ZnS QD are presented in the case of an ideal DOE and the signal acquisition time, optimal from the point of view of tracking (100 ms), depending on the exciting radiation intensity. It is shown that, in the case of QD saturation, the longitudinal coordinate determination accuracy can reach values of ~ 10 nm at exposure times of ~ 100 ms. In addition, we considered the issues of the influence of the experimental parameters (signal acquisition time, power density of the exciting laser radiation, total efficiency of beam conversion into the two-lobe image) on the single QD coordinate reconstruction accuracy. The total efficiency of beam conversion into a two-lobe image is estimated in the case of using a liquid crystal spatial phase modulator of light.

Acknowledgments

Theme AAAA-A19-119083090053-9 of the State Assignment for the Lebedev Physical Institute of the RAS was supported by the Ministry of Science and Higher Education of the Russian Federation. The authors are grateful for support to the Russian Foundation for Basic Research (I T M — grant no. 20-02-00871; D V P, N N L, S P K — grant nos 19-32-90078, 20-02-00671). Studies in the area "Physics of nanostructured materials: fundamental studies and applications in materials science, nanotechnologies, and photonics" were supported by the Ministry of Education of the Russian Federation within the framework of the theme of the State Assignment for Moscow State Pedagogical University (A V N — theme AAAA-20-120061890084-9). A V N, I T M, and I Yu E are members of a Leading Scientific School of the Russian Federation (grant NSh-776.2022.1.2 from the President of the Russian Federation).

References

1. Moerner W E *Angew. Chem. Int. Edit.* **54** 8067 (2015)
2. Betzig E *Angew. Chem. Int. Edit.* **54** 8034 (2015)
3. Hell S W *Angew. Chem. Int. Edit.* **54** 8054 (2015)
4. Möckl L, Moerner W E *J. Am. Chem. Soc.* **142** 17828 (2020)
5. Naumov A, Eremchev I Yu, Gorshelev A A *Eur. Phys. J. D* **68** 348 (2014)
6. Naumov A V *Phys. Usp.* **56** 605 (2013); *Usp. Fiz. Nauk* **183** 633 (2013)
7. Huang B et al. *Science* **319** 810 (2008)
8. Liu L X et al. *Laser Optoelectron. Prog.* **57** 14 (2020)
9. Maiorova A M *Photonics Russia* **12** 134 (2018)
10. Khonina S N et al. *J. Mod. Opt.* **46** 227 (1999)
11. Abramochkin E G, Volostnikov V G *Phys. Usp.* **47** 1177 (2004); *Usp. Fiz. Nauk* **174** 1273 (2004)
12. Pavani S R P, Piestun R *Opt. Express* **16** 22048 (2008)
13. Volostnikov V G *Phys. Usp.* **55** 412 (2012); *Usp. Fiz. Nauk* **182** 442 (2012)
14. Shechtman Y et al. *Nano Lett.* **15** 4194 (2015)
15. Prokopova D V et al. *Bull. Russ. Acad. Sci. Phys.* **83** 1453 (2019); *Izv. Ross. Akad. Nauk Ser. Fiz.* **83** 1612 (2019)
16. Pavani S R P et al. *Proc. Natl. Acad. Sci. USA* **106** 2995 (2009)
17. von Diezmann L, Shechtman Y, Moerner W E *Chem. Rev.* **117** 7244 (2017)

18. Baev A A et al. *Bull. Russ. Acad. Sci. Phys.* **82** 1034 (2018); *Izv. Ross. Akad. Nauk Ser. Fiz.* **82** 1140 (2018)
19. Eremchev I Yu et al. *JETP Lett.* **108** 30 (2018); *Pis'ma Zh. Eksp. Teor. Fiz.* **108** 26 (2018)
20. Möckl L, Roy A R, Moerner W E *Biomed. Opt. Express* **11** 1633 (2020)
21. Razumov V F *Phys. Usp.* **59** 1258 (2016); *Usp. Fiz. Nauk* **186** 1368 (2016)
22. Arzhanov A I et al. *Photonics Russia* **15** 622 (2021)
23. Arzhanov A I et al. *Photonics Russia* **16** 96 (2022)
24. Kulik S I et al. *J. Appl. Spectrosc.* **85** 916 (2018); *Zh. Prikl. Spektrosk.* **85** 814 (2018)
25. Eremchev I Yu, Eremchev M Yu, Naumov A V *Phys. Usp.* **62** 294 (2019); *Usp. Fiz. Nauk* **189** 312 (2019)
26. Razueva E, Abramochkin E *J. Opt. Soc. Am. A* **36** 1089 (2019)
27. Volostnikov V G et al. *Bull. Russ. Acad. Sci. Phys.* **80** 766 (2016); *Izv. Ross. Akad. Nauk Ser. Fiz.* **80** 841 (2016)
28. Vorontsov E N et al. *Bull. Lebedev Phys. Inst.* **45** (3) 71 (2018); *Kr. Soobshch. Fiz.* **45** (3) 9 (2018)
29. Prokopova D V, Kotova S P *Photonics Russia* **14** 170 (2020)
30. Mortensen K I et al. *Nat. Meth.* **7** 377 (2010)
31. Efros A L, Rosen M *Phys. Rev. Lett.* **78** 1110 (1997)
32. Frantsuzov P A, Vólkan-Kacsó S, Jankó B *Phys. Rev. Lett.* **103** 207402 (2009)
33. Osad'ko I S, Eremchev I Yu, Naumov A V *J. Phys. Chem. C* **119** 22646 (2015)